Aerospace Science and Technology, pp. 110533-110533. Article number 110533
DOI:10.1016/j.ast.2025.110533

Modeling multirotor wake interference in quadrotor eVTOL flight dynamics and handling qualities

Yeping Wang[a], Honglei Ji[a, c, *], Linghai Lu[b], Pan Zhou[c]

[a] *College of Aerospace Engineering, Chongqing University, Chongqing 400030, China*

[b] *Flight Dynamic, Simulation and Control Group, Centre for Aeronautics, Cranfield University, Cranfield MK 43 0AL, United Kingdom*

[c] *Key Laboratory of Rotor Aerodynamics, China Aerodynamics Research and Development Center, Mianyang 621000, China*

Abstract

This study presents a good-fidelity flight dynamics model for a quadrotor eVTOL aircraft, with a particular focus on the effects of multirotor aerodynamic interference on vehicle stability and handling qualities. A dynamic vortex tube model, enhanced to account for aircraft angular motions, is developed and integrated with dynamic inflow theory to compute rotor-induced and interference velocities efficiently. The model is validated against wind tunnel data and benchmark trim results, demonstrating strong predictive accuracy. Incorporating this interference model into a 6-DoF flight dynamics framework reveals that multirotor wake interference significantly modify both static and dynamic stability characteristics, especially in low-to-medium speed regimes. Moreover, aerodynamic interference degrades incidence stability, reduces pitch and heave damping, and adversely affects phugoid behavior. In the lateral-directional axes, it destabilizes the spiral mode and introduces non-monotonic variations in Dutch roll stability. Handling qualities analysis using ADS-33E-PRF metrics shows that interference reduces pitch bandwidth from Level 1 to Level 2 and marginally deteriorates pitch and roll dynamic stability, while improving pitch-axis quickness. These findings demonstrate that multirotor aerodynamic interference is not merely a performance issue but a critical factor influencing flight control design and certification. The proposed modeling approach offers a computationally efficient yet physically grounded method for assessing multirotor eVTOL handling qualities across the full flight envelope.

***Keywords*:** quadrotor eVTOL; aerodynamic interference; handling qualities; stability; flight dynamic

I. Introduction

[*]Corresponding author. *E-mail address*: jhl@cqu.edu.cn

Multirotor electric Vertical Take-Off and Landing (eVTOL) aircraft have undergone rapid advancement in recent years, driven by their key advantages such as low environmental impact and highly flexible operational capabilities. These attributes make them strong candidates as foundational elements of future Urban Air Mobility (UAM) systems [1, 2]. Nonetheless, the presence of significant aerodynamic interference among rotors—varying markedly across the flight envelope—presents a persistent challenge. Such interference not only compromises overall aerodynamic efficiency but can also induce severe handling quality (HQ) degradations, occasionally escalating to hazardous flight conditions [3]. As a result, the accurate and efficient evaluation of multirotor interference effects on eVTOL HQs has become a pressing issue in aircraft design and certification [4, 5].

Consequently, the rotorcraft research community has progressively developed a diverse suite of methods and modeling tools aimed at understanding and mitigating aerodynamic interference in multirotor configurations [6-8]. Among the various analytical approaches, Computational Fluid Dynamics (CFD) has emerged as an indispensable tool for studying these complex interactions. Qi et al. [9] developed an efficient CFD-based trim model for coaxial rotors, enabling detailed examination of interference effects on rotorcraft performance. Lakshminarayan et al. [10] investigated coaxial rotor interactions and demonstrated that the upper rotor exhibited significantly greater wake contraction and descent velocity than the lower rotor. Ye et al. [11] employed a multi-layer moving nested grid approach to explore aerodynamic interference between a tiltrotor and its supporting wing in hover, revealing that such interference, compared to the isolated rotor case, generally resulted in increased rotor torques and significant thrust loss at the blade tip regions. Similar investigations into quadrotor configurations [12, 13] found that while interference was negligible during hover in the calm condition, it became pronounced during forward flight. In particular, upstream rotors significantly disrupted the performance of downstream rotors, resulting in a 19% lift reduction and a nose-up pitching moment increase of up to 54%. Stoll and Miki [14] developed a simplified transition aerodynamics model for Joby Aviation's electric tilt-propeller VTOL aircraft by integrating CFD-based propeller surrogate models with semi-empirical airframe and interactional aerodynamics models, validated against both computational and flight test data. This model was then used to analyze transition loads and power requirements under various control strategies. These results highlight the critical importance of accounting for aerodynamic interference when evaluating the HQs of multirotor aircraft.

In addition to CFD, vortex-based methods—well established for rotor wake modeling—have also been widely employed to study interference effects. Bagai and Leishman [15] validated a free vortex wake method by comparing

simulated results for tandem, coaxial, and tiltrotor configurations against wind tunnel data. Building on this, Lee et al. [16] and Alvarez et al. [17] applied the free vortex and viscous vortex particle methods, respectively, to examine aerodynamic interactions in quadrotor systems. Using a vorticity transport model, Brown [18] accurately captured the main rotor wake dynamics, demonstrating how crosswind-induced wake interactions reduce tail rotor thrust [19].

Despite their accuracy, both CFD and high-fidelity vortex methods remain computationally intensive, limiting their practicality for HQs analysis and iterative design studies. To address this, researchers have explored simplified vortex-based approaches tailored for flight dynamics applications. Usov et al. [20] applied the Beddoes generalized wake model in conjunction with dynamic inflow theory to estimate rotor–rotor interference, achieving prediction accuracy within 5% of free wake models while reducing computational cost by two orders of magnitude. Luo et al. [21] introduced a lifting-line based method to model rotor wake systems for fast interference analysis in quadrotors during forward flight, validating their approach through comparison with CFD results. Han et al. [22] further derived an explicit expression for the induced velocity at any spatial point using an equivalent lifting-line model for multiple rotors. Similarly, Divaker [23] developed a multirotor interference model based on a multi-segment horseshoe vortex lifting-line approach, validated against experimental wind tunnel data. However, it is important to note that such models—particularly the generalized wake and equivalent lifting-line approaches—are generally valid only for advance ratios exceeding 0.1. To extend applicability, Guner and Prasad [24] proposed an inflow model for multirotor systems combining momentum theory and a simplified vortex formulation (CMTSVT). While this method demonstrates good fidelity across a range of steady flight conditions, its inability to handle transient effects limits its utility in dynamic stability assessments.

Another solution is to develop empirical or semi-empirical models based on wind tunnel test data or high-fidelity numerical simulation results. Ruddell et al. [25, 26] derived empirical coefficients from wind tunnel and flight tests for flight dynamics modeling of coaxial rigid rotors. Rand et al. [27, 28] linearized the rotor free wake model by applying periodic rotor load excitations, forming a linear dynamic model for coaxial rotor induced velocities. Park et al. [29] augmented the dynamic inflow model by incorporating inflow interference factors identified through the vortex ring wake model [30], enabling fast simulation of multirotor aerodynamic interference effects for flight dynamics modeling. However, this model was only applicable in scenarios where there is no overlap between the rotors. Agarwal et al. [31] proposes an augmented rotor inflow model to capture rotor wake distortions in hover and low-speed flight. Prasad et al. [32, 33] developed an augmented finite-state inflow model based on the superposition

theory of pressure or velocity potential functions to address multirotor aerodynamic interference. The applicability and accuracy of these empirical or semi-empirical models heavily depend on parameter corrections derived from baseline models or wind tunnel test data [34-36]. Their accuracy significantly degrades when applied beyond the conditions for which the parameters were originally defined.

Although numerous multirotor interference models have been developed, most focus on applications related to aerodynamic performance and trim characteristics [21, 37], yet little attention has been given to its influence on flight dynamic modeling and HQs [38-40]. In particular, existing models often treat interference effects as static or quasi-steady phenomena, neglecting the dynamic interactions between rotor wakes and aircraft motions—especially under non-hovering conditions. This limitation hampers the ability to predict and analyze the stability and HQs of multirotor eVTOLs in realistic operational scenarios. To address this gap, this study extends Guner and Prasad's CMTSVT model by incorporating a dynamic vortex tube to account for the influence of aircraft angular rates on rotor wake vortices, enabling its application to stability analysis. On this foundation, a flight dynamics model for a quadrotor eVTOL that accounts for multirotor aerodynamic interference is developed, and the effects of such interference on the HQs of a quadrotor eVTOL are examined.

This paper is organized as follows: Section 1 provides a review of the state-of-the-art research on multirotor interference. Section 2 introduces the multirotor inflow model extended with dynamic vortex tubes. Section 3 presents the flight dynamics model incorporating multirotor interference effects. Section 4 validates both the multirotor interference model and the flight dynamics model. Section 5 systematically analyzes the impact of aerodynamic interference on the HQs of multirotor eVTOL aircraft. Finally, discussion and conclusions are provided.

II. Enhanced multirotor induced velocity model incorporating dynamic vortex tubes

A. Dynamical rotor vortex tube

Building upon classical vortex theory, the rotor system is modeled by assuming an infinite number of blades, with the aerodynamic load distribution across the rotor disk conforming to the Glauert rotor model [41]. Under these conditions, tip vortices shed from the blades propagate downstream indefinitely, driven by the combined effects of the free-stream velocity and rotor-induced velocities. By neglecting both the radial contraction of the vortex wake and the feedback effects from axial velocity components, we establish the proposed vortex-tube wake model, as illustrated in Figure 1.

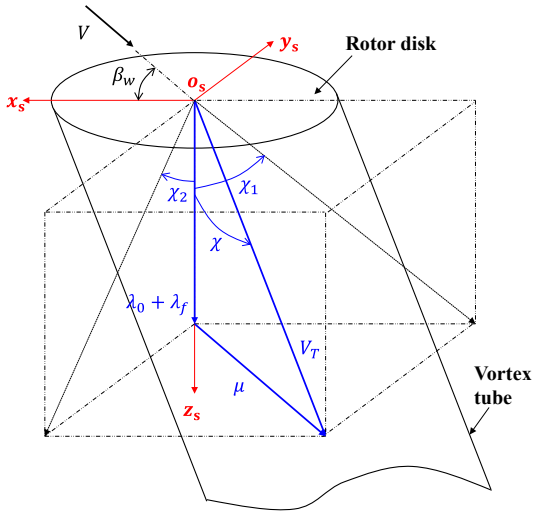

Figure 1 Schematic of rotor vortex tube wake model in rotor shaft axes.

The rotor wake skew angle χ and sideslip angle β_w can be mathematically expressed through the following relationships,

$$\begin{cases} \chi = \tan^{-1}\dfrac{\mu}{\lambda} \\ \beta_w = \tan^{-1}\dfrac{\mu_y}{\mu_x} \end{cases} \tag{1}$$

where λ is the total inflow ratio of the rotor disk plane, μ_x and μ_y denote longitudinal and lateral components of the advance ratio μ along the rotor shaft axes, respectively.

The rotor wake skew angle components χ_1 and χ_2 are obtained by projecting the wake skew angle onto the $x_s z_s$ -plane and $y_s z_s$ -plane, respectively. These components can be expressed as,

$$\begin{cases} \chi_1 = \tan^{-1}\dfrac{\mu_x}{\lambda} \\ \chi_2 = \tan^{-1}\dfrac{\mu_y}{\lambda} \end{cases} \tag{2}$$

By substituting Eq. (2) into Eq. (1) and simplifying, it is gotten that,

$$\begin{cases} \chi = \tan^{-1}\sqrt{\tan^2\chi_1 + \tan^2\chi_2} \\ \beta_w = \tan^{-1}\dfrac{\tan\chi_2}{\tan\chi_1} \end{cases} \tag{3}$$

It is important to note that the aforementioned relationships for rotor wake skew angles do not account for the effects of aircraft angular motions. These angular motions cause the rotor wake to curve during flight. To incorporate

the dynamic effects of the rotor wake, consider the pitch rate as an example. As illustrated in Figure 2, the pitch rate induces curvature in the rotor wake, causing the rotor vortex tube to bend rather than remain straight.

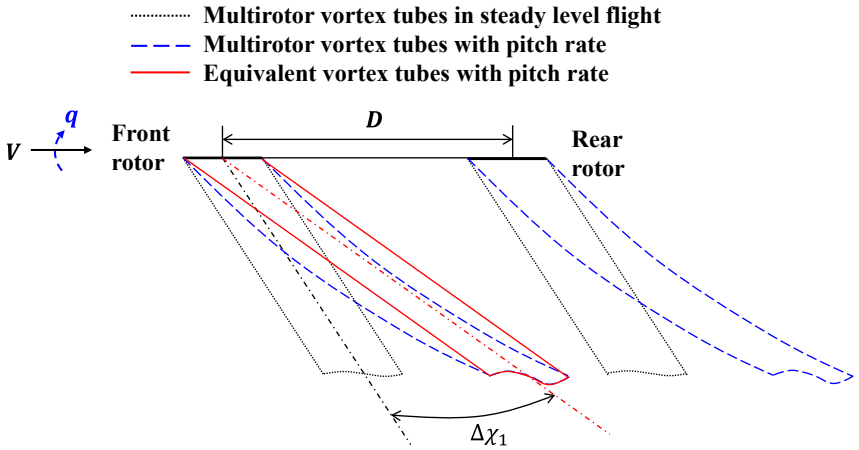

Figure 2 Effect of pitch rate on rotor wake skew angle.

This curved vortex tube can be modeled using an equivalent straight vortex tube, incorporating an additional rotor wake skew angle to account for the effects absent in scenarios without angular motions. This extra rotor wake skew angle $\Delta\chi_1$ can be expressed as,

$$\Delta\chi_1 = k_1 \frac{D}{V_T} q_s \tag{4}$$

where D is the distance between the front and rear rotors, q_s is the pitch rate in the shaft axes, V_T is the total flow velocity through the rotor disk, and k_1 is the time scale factor.

Similarly, when considering the roll rate of the aircraft, the additional rotor wake skew angle $\Delta\chi_2$ is,

$$\Delta\chi_2 = k_2 \frac{D}{V_T} p_s \tag{5}$$

where p_s is the roll rate and k_2 is the time scale factor.

Taking into account the additional rotor wake skew angles induced by aircraft angular motions, the effective wake angle and sideslip angle can be expressed as follows,

$$\begin{cases} \chi' = \tan^{-1}\sqrt{\tan^2(\chi_1+\Delta\chi_1)+\tan^2(\chi_2+\Delta\chi_2)} \\ \beta'_w = \tan^{-1}\dfrac{\tan(\chi_2+\Delta\chi_2)}{\tan(\chi_1+\Delta\chi_1)} \end{cases} \tag{6}$$

Based on the dynamic straight rotor vortex tube model, the induced velocity at any spatial location $P(x,y,z)$ can be calculated using the Biot-Savart law [42] as follows,

$$\begin{cases} \overline{u} = -\dfrac{1}{4\pi}\int_0^{2\pi} \gamma(\psi) \dfrac{\overline{z}\cos\psi + \overline{R}_c \cos\chi'\cos\psi}{\left(\overline{R}_c + \overline{z}\cos\chi' - \overline{x}\sin\chi' + \sin\chi'\cos\psi\right)\overline{R}_c} d\psi \\ \overline{v} = -\dfrac{1}{4\pi}\int_0^{2\pi} \gamma(\psi) \dfrac{\overline{z}\sin\psi + \overline{R}_c \cos\chi'\sin\psi}{\left(\overline{R}_c + \overline{z}\cos\chi' - \overline{x}\sin\chi' + \sin\chi'\cos\psi\right)\overline{R}_c} d\psi \\ \overline{w} = -\dfrac{1}{4\pi}\int_0^{2\pi} \gamma(\psi) \dfrac{1 - \overline{x}\cos\psi - \overline{y}\sin\psi + \overline{R}_c \sin\chi'\cos\psi}{\left(\overline{R}_c + \overline{z}\cos\chi' - \overline{x}\sin\chi' + \sin\chi'\cos\psi\right)\overline{R}_c} d\psi \end{cases} \tag{7}$$

where $\overline{u},\overline{v},\overline{w}$ are the normalized induced velocity components, ψ is the azimuth angle in the rotor plane, $\overline{x},\overline{y}$ and $\overline{z}$ are the normalized coordinates of point P, and $\overline{R}_c$ is

$$\overline{R}_c = \sqrt{\overline{R}^2 + \overline{x}^2 + \overline{y}^2 + \overline{z}^2 - 2\left(\overline{x}\cos\psi + \overline{y}\sin\psi\right)}$$

$\gamma(\psi)$ is the vortex strength distribution along the azimuth angle,

$$\gamma(\psi) = \overline{\gamma}_0 + \overline{\gamma}_{1c}\cos\psi + \overline{\gamma}_{1s}\sin\psi$$

The mean and harmonic components of the vortex strength can be determined based on their relationship with the rotor's aerodynamic thrust, roll moment, and pitch moment, as described by the following equations [43],

$$\begin{cases} \overline{\gamma}_0 = \dfrac{C_T + 3\mu C_L}{\overline{V}_T\left(1 - 1.5\mu^2\right)} \\ \overline{\gamma}_{1c} = -\dfrac{3C_M}{\overline{V}_T} \\ \overline{\gamma}_{1s} = -\dfrac{1.5\mu C_T + 3C_L}{\overline{V}_T\left(1 - 1.5\mu^2\right)} \end{cases} \tag{8}$$

where C_T, C_L and C_M are the thrust, roll, and pitch moment coefficients, respectively, and $\overline{V}_T$ is the normalized inflow velocity of the rotor disk.

To resolve the singularities encountered in Eq. (7) during the calculation of interference velocity for points in proximity to the vortex tube wall, a first-order Vatistas vortex core model [44] is utilized to reformulate the induced velocity computation,

$$\overline{R}_c = \sqrt{\overline{R}^2 + \overline{x}^2 + \overline{y}^2 + \overline{z}^2 + \delta^2 - 2\left(\overline{x}\cos\psi + \overline{y}\sin\psi\right)} \tag{9}$$

where δ is the non-dimensional vortex core radius.

Consequently, a dynamic rotor vortex tube model is developed to accurately characterize multirotor interference effects.

B. Multirotor induced velocity model

Utilizing the dynamic rotor vortex tube model, the aerodynamic interference velocity between any pair of rotors can be quantitatively determined. As illustrated in Figure 3, consider a system comprising two rotors, denoted as R_i and R_j. The center of the R_i is located at coordinates (x_{hi}, y_{hi}, z_{hi}) within the body coordinate system, characterized by the lateral tilt angle ϕ_i and the longitudinal tilt angle θ_i relative to the fuselage. The shaft coordinate system $o_{hi} - x_{si}y_{si}z_{si}$ is defined such that the $x_{si}y_{si}$-plane is vertical to the rotor shaft axis, where the x_{si}-axis is oriented rearward (positive direction), the z_{si}- axis is directed upward (positive direction), and the y_{si}-axis is determined by the right-hand rule. The wind coordinate system can be obtained by rotating the rotor shaft coordinate system through the sideslip angle β_{wi}, such that its x_{wi}-axis aligns with the freestream velocity direction. Following the same methodology, the shaft coordinate system and the wind coordinate system for R_j can be analogously defined.

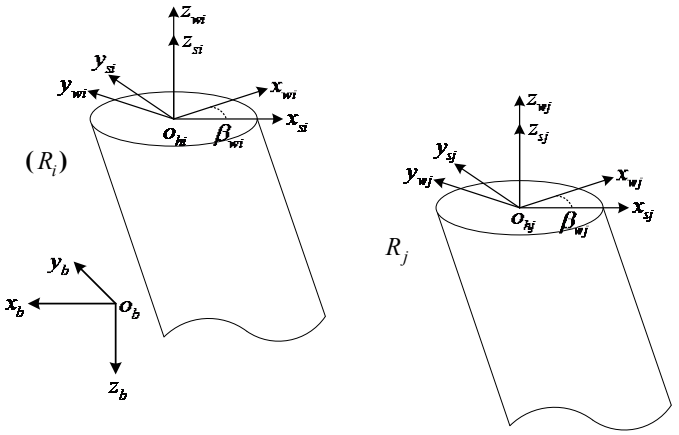

Figure 3 Schematic of rotor/rotor aerodynamic interference.

Assume that the radial distance from an arbitrary point Q on the shaft plane of R_i to center is r, and the azimuth angle is ψ. Based on the relative geometric relationship between R_i and R_j, the coordinates of the point Q in the wind coordinate system of R_j can be expressed as,

$$\begin{bmatrix} x_{Qwj} \\ y_{Qwj} \\ z_{Qwj} \end{bmatrix} = \boldsymbol{T}_{sj}^{wj} \boldsymbol{T}_{b}^{sj} \left\{ \boldsymbol{T}_{si}^{b} \begin{bmatrix} r\cos\psi \\ r\sin\psi \\ 0 \end{bmatrix} + \begin{bmatrix} x_{hi} \\ y_{hi} \\ z_{hi} \end{bmatrix} - \begin{bmatrix} x_{hj} \\ y_{hj} \\ z_{hj} \end{bmatrix} \right\} \tag{10}$$

where $\boldsymbol{T}_{si}^{b}$ is the coordinate transformation matrix from the shaft coordinate system of R_i to the aircraft body coordinate system,

$$\boldsymbol{T}_{si}^{b}=\begin{bmatrix}-\cos\phi_i & 0 & \sin\phi_i\\ \sin\phi_i\sin\theta_i & \cos\phi_i & \sin\phi_i\cos\theta_i\\ -\cos\phi_i\sin\theta_i & \sin\phi_i & -\cos\phi_i\cos\theta_i\end{bmatrix} \tag{11}$$

$\boldsymbol{T}_{b}^{sj}$ is the coordinate transformation matrix from the aircraft body coordinate system to the shaft coordinate system of R_j, equal to the transpose of $\boldsymbol{T}_{sj}^{b}$, and $\boldsymbol{T}_{sj}^{wj}$ is the coordinate transformation matrix from the shaft coordinate system of R_j to the wind coordinate system,

$$\boldsymbol{T}_{sj}^{wj}=\begin{bmatrix}\cos\beta_{wj} & \sin\beta_{wj} & 0\\ -\sin\beta_{wj} & \cos\beta_{wj} & 0\\ 0 & 0 & 1\end{bmatrix} \tag{12}$$

Given the coordinates, the interference velocity at point Q due to the vortex system of R_j can be calculated and expressed as u_{Qwj}, v_{Qwj} and w_{Qwj}. By transforming these velocity components into the shaft coordinate system of R_i, The induced velocity at point Q on R_i due to R_j is,

$$\begin{bmatrix}u_{si}\\ v_{si}\\ w_{si}\end{bmatrix}=\boldsymbol{T}_{b}^{si}\boldsymbol{T}_{sj}^{b}\boldsymbol{T}_{wj}^{sj}\begin{bmatrix}u_{Qwj}\\ v_{Qwj}\\ w_{Qwj}\end{bmatrix} \tag{13}$$

where $\boldsymbol{T}_{wj}^{sj}$ is the coordinate transformation matrix from the wind coordinate system of R_j to the shaft coordinate system, $\boldsymbol{T}_{sj}^{b}$ is the coordinate transformation matrix from the shaft coordinate system of R_j to the aircraft body coordinate system, and $\boldsymbol{T}_{b}^{si}$ is the coordinate transformation matrix from the aircraft body coordinate system to the shaft coordinate system of R_i.

By integrating the induced velocity from rotor to rotor, along the radial and azimuthal directions, the aerodynamic interference velocity components of R_j acting on R_i can be obtained as follows,

$$\begin{cases} \lambda_0^{I_{qs}} = -\dfrac{1}{\Omega R}\dfrac{1}{\pi R^2}\int_0^{2\pi}\int_0^R w_{si}(r,\psi)\,r dr d\psi \\ \lambda_{1c}^{I_{qs}} = -\dfrac{1}{\Omega R}\dfrac{4}{\pi R^3}\int_0^{2\pi}\int_0^R w_{si}(r,\psi)\,r^2\cos\psi\, dr d\psi \\ \lambda_{1s}^{I_{qs}} = -\dfrac{1}{\Omega R}\dfrac{4}{\pi R^3}\int_0^{2\pi}\int_0^R w_{si}(r,\psi)\,r^2\sin\psi\, dr d\psi \end{cases} \tag{14}$$

$$\begin{cases} \mu_x^{I_{qs}} = \dfrac{1}{\Omega R}\dfrac{1}{\pi R^2}\int_0^{2\pi}\int_0^R u_{si}(r,\psi)\,r dr d\psi \\ \mu_y^{I_{qs}} = \dfrac{1}{\Omega R}\dfrac{1}{\pi R^2}\int_0^{2\pi}\int_0^R v_{si}(r,\psi)\,r dr d\psi \end{cases} \tag{15}$$

where Ω denotes the rotor speed, R represents the rotor radius, $\lambda_0^{I_{qs}}$ is the mean value of the normalized vertical interference velocity, $\lambda_{1s}^{I_{qs}}$ and $\lambda_{1c}^{I_{qs}}$ are the first-order harmonic components of the normalized vertical interference velocity, while $\mu_x^{I_{qs}}$ and $\mu_y^{I_{qs}}$ correspond to the normalized longitudinal and lateral interference velocity components, respectively.

A first-order delay is introduced to capture the dynamic effects of aerodynamic interference between the rotors,

$$\tau_I \begin{bmatrix} \dot{\lambda}_0^I \\ \dot{\lambda}_{1c}^I \\ \dot{\lambda}_{1s}^I \\ \dot{\mu}_x^I \\ \dot{\mu}_x^I \end{bmatrix} + \begin{bmatrix} \lambda_0^I \\ \lambda_{1c}^I \\ \lambda_{1s}^I \\ \mu_x^I \\ \mu_x^I \end{bmatrix} = \begin{bmatrix} \lambda_0^{I_{qs}} \\ \lambda_{1c}^{I_{qs}} \\ \lambda_{1s}^{I_{qs}} \\ \mu_x^{I_{qs}} \\ \mu_x^{I_{qs}} \end{bmatrix} \tag{16}$$

where $\tau_I = D/V$ is the time constant.

The dynamic inflow model [45] is utilized to determine the self-induced velocity for each individual rotor, with its dynamic characteristics captured by the following governing equation,

$$\frac{1}{\Omega}\boldsymbol{\tau}\begin{bmatrix} \dot{\lambda}_0^S \\ \dot{\lambda}_{1s}^S \\ \dot{\lambda}_{1c}^S \end{bmatrix} + \begin{bmatrix} \lambda_0^S \\ \lambda_{1s}^S \\ \lambda_{1c}^S \end{bmatrix} = \boldsymbol{L}\begin{bmatrix} C_T \\ C_L \\ C_M \end{bmatrix} \tag{17}$$

in which the superscript S represents self-induced velocity components, and the associated matrices $\boldsymbol{\tau}$ and $\boldsymbol{L}$ can be expressed as,

$$\boldsymbol{\tau}=\begin{bmatrix} \dfrac{4}{3\pi\bar{V}_T} & 0 & -\dfrac{1}{12\bar{V}_M}\tan\dfrac{\chi}{2} \\ 0 & -\dfrac{64}{45\pi\bar{V}_M\left(1+\cos\chi\right)} & 0 \\ \dfrac{5}{8\pi\bar{V}_T}\tan\dfrac{\chi}{2} & 0 & \dfrac{64\cos\chi}{45\pi\bar{V}_M\left(1+\cos\chi\right)} \end{bmatrix} \tag{18}$$

$$\boldsymbol{L}=\begin{bmatrix} \dfrac{1}{2\bar{V}_T} & 0 & \dfrac{15\pi}{64\bar{V}_M}\tan\dfrac{\chi}{2} \\ 0 & -\dfrac{4}{\bar{V}_M\left(1+\cos\chi\right)} & 0 \\ \dfrac{15\pi}{64\bar{V}_T}\tan\dfrac{\chi}{2} & 0 & -\dfrac{4\cos\chi}{\bar{V}_M\left(1+\cos\chi\right)} \end{bmatrix} \tag{19}$$

where $\bar{V}_M$ is the mass flow parameter.

Finally, the total induced velocity for each rotor in the multirotor system can be obtained through the superposition of the interference velocity derived from Eq. (16) and the self-induced velocity calculated from Eq. (17),

$$\begin{cases} \lambda_0=\lambda_0^S+\lambda_0^I \\ \lambda_{1s}=\lambda_{1s}^S+\lambda_{1s}^I \\ \lambda_{1c}=\lambda_{1c}^S+\lambda_{1c}^I \end{cases} \tag{20}$$

III. Flight dynamics model

NASA's quadrotor configuration [37], specifically optimized for single-passenger transport, serves as the baseline for a detailed investigation into aerodynamic performance, stability characteristics, and HQs. The conceptual layout of the design, including the spatial arrangement of critical components, is presented in Figure 4. The vehicle employs an electric propulsion system designed to carry a 113 kg payload over an operational range of 92.6 km. To meet the unique requirements of UAM operations, the flight dynamics model integrates rotor flapping dynamics with a comprehensive collective pitch control strategy. The control system generates roll motion through differential collective pitch between the left-side rotor group (Rotors 2 and 3) and right-side rotor group (Rotors 1 and 4), while pitch control is achieved via differential collective pitch between the front rotor pair (Rotors 1 and 2) and rear rotor pair (Rotors 3 and 4). Yaw control is implemented through differential collective pitch across diagonal rotor pairs, completing this triaxial control strategy that provides full attitude authority while maintaining mechanical simplicity.

The inclusion of rotor flapping effects ensures accurate modeling of rotor dynamics during complex UAM flight maneuvers.

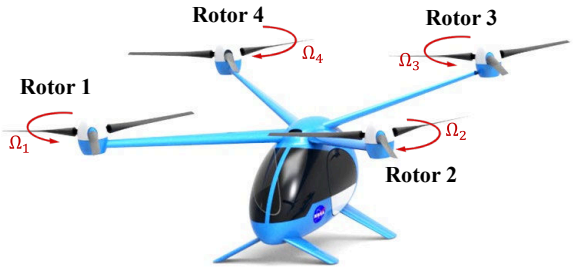

Figure 4 Single-passenger quadrotor aircraft [37].

Building upon the established multirotor induced velocity model, the blade element method is utilized for rotor aerodynamic calculations [46, 47], while rotor flapping motion is determined through the moment equilibrium equation at the flapping hinge [48]. Fuselage aerodynamics are characterized using simplified aerodynamic coefficients following the approach described in Ref. [38], with rotor interference effects on the airframe considered negligible. The motor response time constant for this quadrotor is approximately 0.24 s [49]. The complete flight dynamics model incorporates rigid body 6-degree-of-freedom (DoF) equations of motion, employing a total of 60 state variables to capture the nonlinear dynamic behavior encompassing rigid body motion, rotor flapping dynamics, and multirotor induced velocity effects. Referring to the derivations in Refs. [50-53], the comprehensive nonlinear system is represented by the following full-state equations,

$$\dot{\boldsymbol{x}} = f(\boldsymbol{x}, \boldsymbol{u}) \tag{21}$$

where $\boldsymbol{x}$ represents the state vector of the system,

$$\boldsymbol{x} = \begin{bmatrix} & & & \phi & \theta & \psi & p & q & r & u & v & w & x & y & z & & & \\ \dot{a}_{0,i} & \dot{a}_{1,i} & \dot{b}_{1,i} & a_{0,i} & a_{1,i} & b_{1,i} & \lambda_{0,i}^{S} & \lambda_{1c,i}^{S} & \lambda_{1s,i}^{S} & \lambda_{0,i}^{I} & \lambda_{1c,i}^{I} & \lambda_{1s,i}^{I} \end{bmatrix}^{T}, i = 1,2,3,4 \tag{22}$$

in which ϕ, θ, ψ represent the Euler angles (roll, pitch, and yaw, respectively); p, q, r denote the angular rates in the body frame; u, v, w correspond to the body-axis translational velocity components; x, y, z denote the displacement components in the inertial frame; $a_{0,i}, a_{1,i}, b_{1,i}$ and $\dot{a}_{0,i}, \dot{a}_{1,i}, \dot{b}_{1,i}$ are the flap angles and flap angular rates of R_i, while $\lambda_{0,i}^{S}, \lambda_{1c,i}^{S}, \lambda_{1s,i}^{S}$ and $\lambda_{0,i}^{I}, \lambda_{1c,i}^{I}, \lambda_{1s,i}^{I}$ represent its self-induced velocity and mutual interference velocity components, respectively.

$\boldsymbol{u}$ represents the control input vector,

$$\boldsymbol{u} = \begin{bmatrix} \delta_{col} & \delta_{lat} & \delta_{lon} & \delta_{ped} \end{bmatrix}^T \tag{23}$$

in which δ_{col} represents collective pitch control input, δ_{lat} represents lateral control input, δ_{lon} represents longitudinal control input, and δ_{ped} represents yaw control input.

IV. Validation

This section first validates the implemented induced velocity model, followed by the verification of the flight dynamics model.

A. Multirotor induced velocity model validation

The multirotor-induced velocity model is validated against wind tunnel test data from a tandem rotor configuration, with a focus on quantifying the aerodynamic interference effects between the front and rear rotors. In the experiments, the thrust coefficients of both rotors were maintained at a constant value of 0.0034, while the required power was measured to evaluate rotor-rotor interference effects [54]. Additional validation parameters are detailed in Table 1. The total induced velocity was computed using the multirotor-induced velocity model, and the required power—comprising induced power, profile drag power, and parasitic drag power [55]—was calculated as follows,

$$C_P = \kappa C_T \lambda_0 + \frac{\sigma C_d}{8}\left(1 + 4.65\mu^2\right) + \frac{1}{4}\mu^3 \frac{f}{A} \tag{24}$$

where κ is the induced power correction factor, σ is the rotor solidity, C_d is the drag coefficient of the rotor blade airfoil, and f is the equivalent flat plane drag area.

Table 1 Primary rotor parameters for validation against wind tunnel test data in Ref. [54]

Parameter	Value	Parameter	Value
Rotor radius (m)	2.286	Tip speed (m/s)	152.4
Longitudinal spacing of rotors (m)	2.06 R	Vertical spacing of rotors (m)	0
Induced power correction factor	1.200	Rotor solidity	0.054
Equivalent flat plane drag area (m^2)	0.186	Airfoil drag coefficient	0.010

Figure 5 presents a comparison of the level-flight performance of the front and rear rotors, as predicted by the proposed tandem rotor-induced velocity model, against corresponding wind tunnel measurements. To further elucidate

the effects of multirotor aerodynamic interference on inflow velocities, the figure also includes single-rotor results, representing a non-interfering baseline condition.

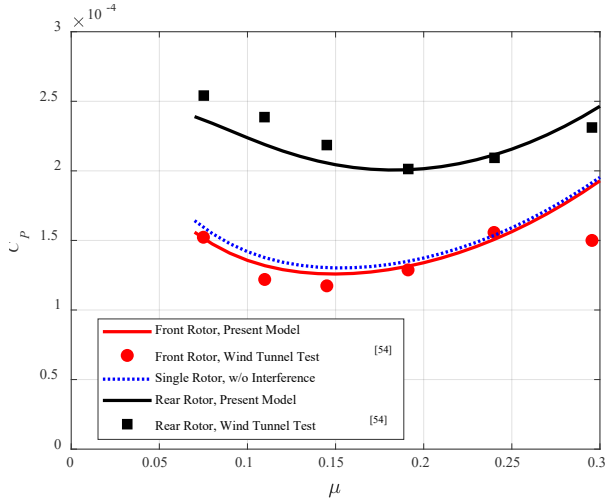

Figure 5 Comparison of required power coefficients with flight speed for tandem rotor configuration.

From Figure 5, it can be observed that the results from the present model are generally well aligned with the wind tunnel test data and follow the typical rotorcraft power trend, while the test data from Ref. [54] do not adhere to this trend at the highest speed. Additionally, compared to the single rotor without interference, the front rotor is almost unaffected by interference, while the required power of the rear rotor increases significantly, indicating a more severe interference effect on the rear rotor.

An additional validation was performed using tandem rotor wind tunnel test data from Ref. [56]. In this experimental setup, both front and rear rotors maintained the same collective pitch angle as the baseline single rotor configuration. The thrust and torque of the rear rotor were systematically recorded across all test conditions to evaluate system performance. The total induced velocity was calculated using the multirotor inflow velocity model incorporating the measured thrust coefficients. The required power for the rear rotor was then computed using Eq.(24), with the results compared against experimental data for validation. Table 2 summarizes the key parameters of the tandem rotor configuration used in these calculations. For this configuration, the rotor blade airfoil drag coefficient is expressed as,

$$C_d = \delta_0 + \delta_2 \alpha^2 \tag{25}$$

where δ_0 and δ_2 represent the zero-lift drag coefficient and the induced drag factor of the airfoil, respectively, and α is the equivalent angle of attack, as defined by [24],

$$\alpha = \frac{6C_T}{\sigma\alpha_\infty} \tag{26}$$

where α_∞ is the lift curve slope of the airfoil.

Table 2 Primary rotor parameters for validation against wind tunnel test data in Ref. [56]

Parameter	Value	Parameter	Value
Rotor radius (m)	1.020	Tip speed (m/s)	128.18
Longitudinal spacing of rotors (m)	1.8 R	Vertical spacing of rotors (m)	0.2 R
Induced power correction factor	1.200	Rotor solidity	0.037
Airfoil's lift curve slope (rad^{-1})	5.730	Airfoil zero-lift drag coefficient	0.008
Airfoil's induced drag factor	0.400	Equivalent flat plane drag area	0

Figure 6 compares the power - thrust coefficient characteristics of the rear rotor, as predicted by the present model, with wind tunnel data across a range of advance ratios. The figure also includes computational results and experimental measurements for an isolated single-rotor configuration, in which aerodynamic interference effects are absent. As evident from the figure, the front rotor's wake exerts a pronounced influence on the rear rotor's performance, notably reducing thrust output and increasing power consumption under identical collective pitch settings. These interference effects become more pronounced with increasing thrust coefficients. The proposed model shows strong agreement with wind tunnel results for both the isolated single-rotor and rear-rotor configurations, with prediction errors remaining within 15% across all test conditions. In the single-rotor case, the primary source of difference arises from the model's neglect of advance ratio influences on the induced power correction factor. For the rear rotor, the dominant difference is associated with the use of front rotor thrust coefficients derived from isolated rotor test data, which inherently neglects reverse interference effects from the rear rotor. This modelling simplification limits the accuracy of interference quantification between the two rotors.

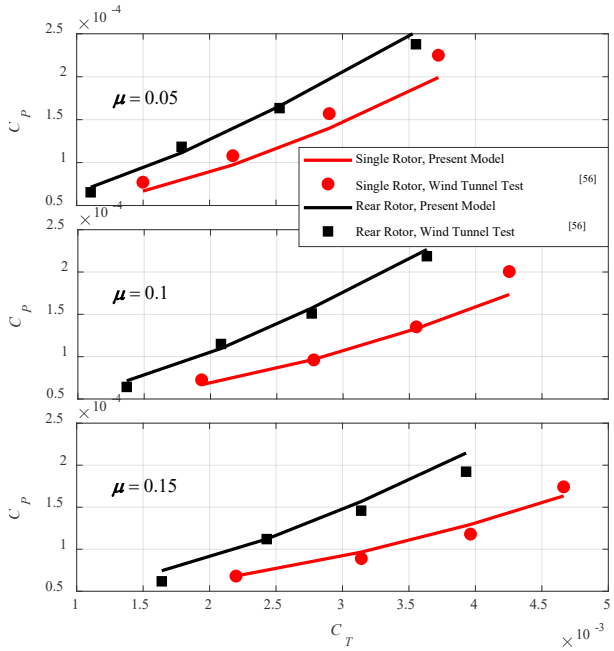

Figure 6 Comparison of required power coefficients with thrust coefficients for tandem rotor configuration.

B. Flight dynamics model verification

The flight dynamics model is verified through comparison of trim results for the quadrotor aircraft across the full speed envelope (0 - 70 m/s) against benchmark data from Johnson and Silva [37]. Table 3 summarizes the key design parameters of the quadrotor configuration used in this analysis [49, 57], which features a staggered rotor arrangement with the rear rotors positioned vertically higher than the front rotors, as shown in Figure 4.

Table 3 Key design parameters of quadrotor configuration

Parameter	Value	Parameter	Value
Design gross weight (kg)	600.92	CG coordinates (m)	(0.1208, 0, 0.2743)
Rotor mass static moment ($\mathrm{kg \cdot m^2}$)	4.8605	Rotor radius (m)	1.9812
Rotor moment of inertia ($\mathrm{kg \cdot m^2}$)	6.3210	Tip speed (m/s)	137.16
Rotor solidity	0.0650	Blade twist (°)	-12
Moment of inertia about x-axis ($\mathrm{kg \cdot m^2}$)	1056.8	Lateral spacing of rotors (m)	2.7 R
Moment of inertia about y-axis ($\mathrm{kg \cdot m^2}$)	1153.6	Longitudinal spacing of rotors (m)	2.7 R
Moment of inertia about z-axis ($\mathrm{kg \cdot m^2}$)	1359.8	Vertical spacing of rotors (m)	0.35 R

Figure 7 presents a comparative analysis of front and rear rotor thrust variations with forward flight speed between the proposed flight dynamics model and reference data from Ref. [37]. The results indicate that as forward speed increases, the front rotor thrust decreases while the rear rotor thrust increases. At low speeds, the front rotor produces higher thrust to counteract the nose-down pitching moment induced by the vehicle's forward-located center of gravity (CG), thereby maintaining longitudinal trim. As flight speed increases, the fuselage's aerodynamic surfaces produce progressively larger stabilizing nose-up moments, thereby reducing the required contribution from the front rotors. Concurrently, the rear rotor thrust must increase to maintain overall moment balance. The model's predicted thrust variations show excellent agreement with the reference data across the entire speed range, validating its ability to accurately characterize the rotor thrust distribution under varying flight conditions.

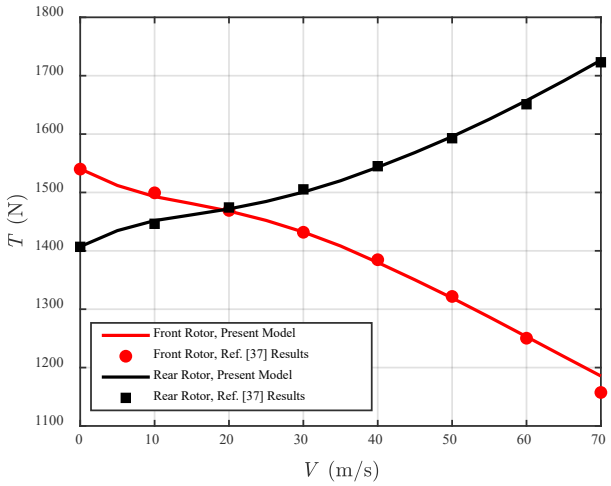

Figure 7 Comparison of front and rear rotor thrust variations with flight speed.

Figure 8 presents a comparative analysis of the power requirements for the front and rear rotors, with and without consideration of multirotor aerodynamic interference. The model predictions that account for interference effects exhibit strong agreement with the reference data, with a maximum deviation of only 8.03%. This close correspondence not only validates the fidelity of the flight dynamics model but also confirms its capability to accurately capture aerodynamic interactions between rotors during flight. Relative to the non-interference case, the inclusion of aerodynamic coupling introduces distinct power redistribution: the front rotor shows a modest reduction in power demand, while the rear rotor requires significantly more power. This shift is attributed to the downstream convection of the front rotor's vortex wake, which increases the inflow velocity at the rear rotor and, in turn, its power consumption. Concurrently, the rear rotor's induced flow alters the wake trajectory of the front rotor, drawing it further downstream and thereby reducing the front rotor's inflow and associated power requirement.

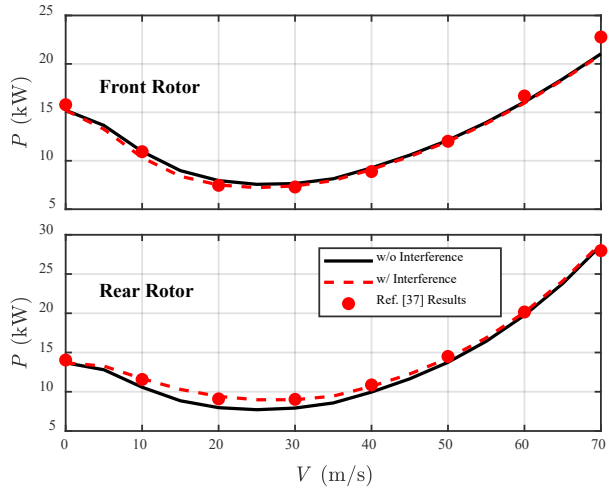

Figure 8 Comparison of power requirements for front and rear rotors with flight speed.

The lateral symmetry of the eVTOL configuration necessitates zero lateral/yaw control inputs and neutral attitudes in trimmed flight. Thus, only longitudinal dynamics are presented to characterize multirotor interference effects. Figure 9 compares the pitch attitude, collective pitch, and longitudinal control inputs required for trimmed flight, with and without accounting for multirotor aerodynamic interference. The results indicate that the vehicle adopts an increasingly nose-down pitch attitude as forward flight speed increases. This behavior stems from the quadratic growth of fuselage drag with airspeed, which necessitates a greater nose-down orientation to generate sufficient horizontal force from the rotor system to counteract the drag force. Notably, the pitch angle decreases to as much as -14° at maximum forward speed, in agreement with the prediction in Ref. [58], a result primarily stemming from the intrinsic limitations of the quadrotor configuration. The inclusion of multirotor aerodynamic interference has a negligible effect on the pitch angle trend. This is primarily because the current model does not incorporate aerodynamic interactions between the rotors and the fuselage, limiting its sensitivity to such interference in pitch dynamics.

The collective pitch control follows a characteristic “bucket curve” with flight speed, reaching a minimum at the speed where induced and parasitic power components balance. Multirotor aerodynamic interactions introduce a slight elevation in collective requirements at transitional speeds (20 - 40 m/s), as rear rotors experience greater induced velocities due to wake ingestion from forward rotors. In contrast, the interference has more pronounced effects on longitudinal control: the front rotors experience reduced inflow velocity as their wake is displaced by the rear rotors’ induced flow, while the rear rotors encounter increased inflow velocity as they ingest the front rotors’ wakes.

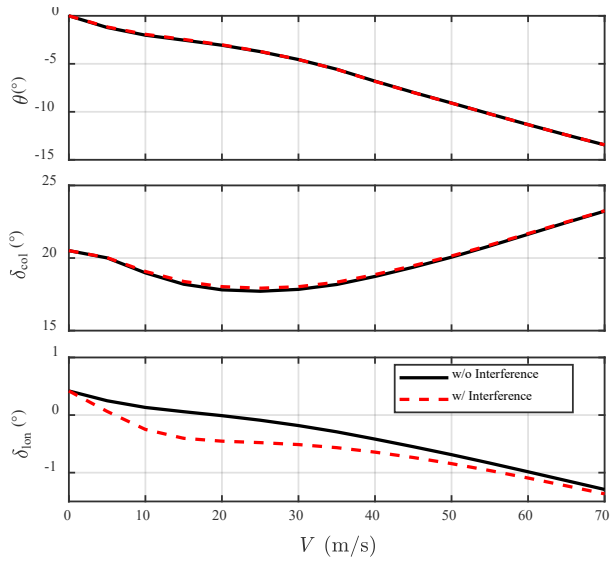

Figure 9 Comparison of pitch attitude, collective pitch, and longitudinal control inputs for trimmed flight.

V. Effects of multirotor interference on the handling qualities of eVTOL

A. Stability analysis

To better understand the influence of multirotor aerodynamic interactions on flight dynamics, this Section examines their effects on both stability derivatives and HQs across a range of forward flight speeds. A linearized model is used to evaluate how interference between rotor wakes modifies key aerodynamic characteristics, particularly in low- to moderate-speed regimes. The analysis explores changes in static and dynamic stability modes, root locus behavior, and control responsiveness, with a focus on identifying performance implications relevant to ADS-33E-PRF HQs criteria [59]. This investigation provides a foundation for assessing the broader stability and control challenges posed by multirotor configurations in advanced eVTOL designs.

1. Static stability

Figure 10 and Figure 14 illustrate how aerodynamic interference among rotors in a quadrotor configuration affects key static stability derivatives as a function of forward flight speed. Each subplot compares the behavior of a given derivative with and without multirotor aerodynamic interference, shedding light on how wake interactions impact vehicle stability [60].

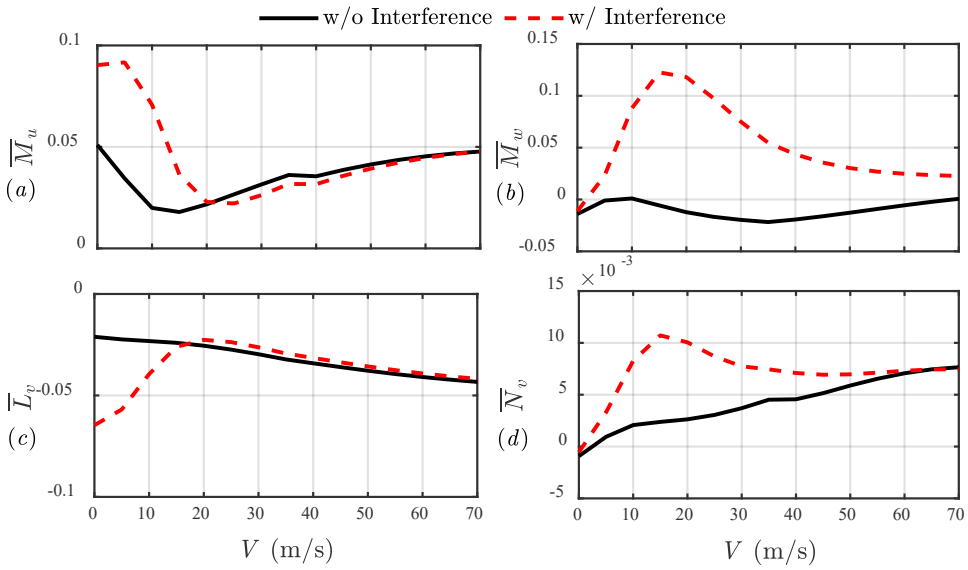

Figure 10 Comparison of static derivatives with flight speed: (*a*) speed stability derivative ($\overline{M}_u$), (*b*) incidence stability derivative ($\overline{M}_w$), (*c*) dihedral derivative ($\overline{L}_v$), and (*d*) weathercock derivative ($\overline{N}_v$).

Figure 10 (*a*) and (*c*) illustrate that multirotor aerodynamic interference has a pronounced effect on both $\overline{M}_u$ and $\overline{L}_v$ at low flight speeds. The qualitative trends of these derivatives align well with those observed in conventional rotorcraft such as the Lynx and Puma, as documented by Padfield [4], where the rotor-induced moments remain relatively constant while fuselage contributions vary significantly with forward speed. In the case of the present quadrotor configuration—lacking a horizontal tail surface, as shown in Figure 4—the equivalent stabilizing influence originates from the front rotor system. The sharp variation in $\overline{M}_u$ below 20 m/s is attributed to the rearward tilting of the front rotor wakes with increasing velocity, which intensifies downwash on the rear rotors and produces a stronger nose-up pitching moment. This behavior is analogous to the increased pitch moment experienced by conventional helicopters due to main rotor downwash loading the horizontal stabilizer (Padfield [4], Chapter 4). As the vehicle's longitudinal increases, the upstream rotor wakes are further deflected downstream, as depicted in Figure 11. This wake deflection enhances interference on downstream rotors, thereby amplifying pitch moment. Consequently, multirotor interference strengthens longitudinal speed stability in low-speed regimes. However, as forward speed increases, rotor wakes align more consistently with the freestream, reducing wake overlap and aerodynamic coupling. The resulting attenuation in interference effects causes the derivatives to converge with those of the non-interference case at higher speeds.

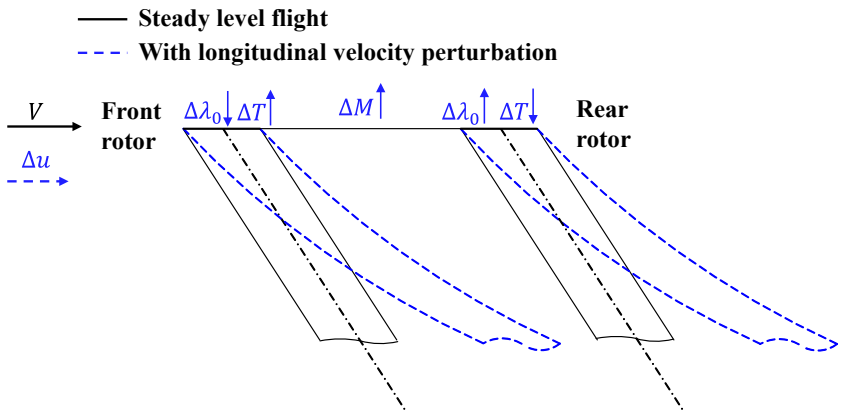

Figure 11 Impact of longitudinal velocity perturbation on pitch moment.

A similar explanation can be provided for $\bar{L}_v$ in Figure 10 (*c*) which describes how roll moment responds to sideslip velocity. With interference, $\bar{L}_v$ is significantly more negative at low speeds, reflecting an enhanced dihedral effect. In a quadrotor, this results from asymmetric wake deflection during lateral motion: the upstream rotor wake interferes more with the downstream rotor, increasing rolling moments that oppose sideslip. Padfield highlights a similar mechanism for helicopters, where tail rotor or side-force generator interactions yield dihedral-like contributions in lateral flight.

Figure 10 (*b*) highlights a notable reversal in the incidence stability derivative $\bar{M}_w$, which shifts from negative to positive when multirotor aerodynamic interference is considered—signifying a transition from static stability to static instability. This behavior arises from the coupled influence of rotor thrust moment contributions unique to multirotor systems. In the absence of aerodynamic interference, although both the rotors and fuselage are inherently prone to incidence instability, similar to conventional rotorcraft, the quadrotor configuration, featuring a forward CG and no empennage (see Figure 4), maintains overall static stability due to the dominant stabilizing contribution from rotor thrust moments. However, incorporation of aerodynamic interference effects leads to substantial variations in the flight dynamics characteristics throughout the operational flight envelope. An increase in angle of attack leads to pronounced rearward deflection of the front rotor wakes, as illustrated in Figure 12. This deflection intensifies the downwash on the rear rotors, reducing their effective thrust and inducing a destabilizing nose-up moment. The resultant destabilization overwhelms the stabilizing contribution from the forward CG, particularly at moderate flight speeds where interference is strongest. This mechanism mirrors high-wash interference effects observed in conventional rotorcraft, such as the rotor hub wake impingement described by Padfield. Overall, across the full flight speed envelope, the net effect is a clear degradation of incidence stability, with $\bar{M}_w$ becoming positive under

interference—highlighting the importance of wake-induced coupling in shaping pitch stability characteristics in multirotor flight dynamics.

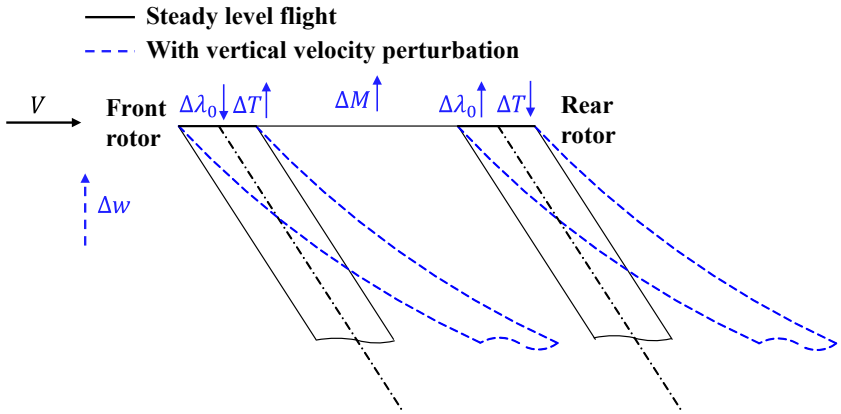

Figure 12 Impact of vertical velocity perturbation on pitch moment.

Figure 10 (*d*) shows that multirotor aerodynamic interference leads to a clear increase in $\bar{N}_v$, particularly in the low-to-medium speed regime. This derivative reflects the aircraft's tendency to realign with the relative airflow following a lateral velocity perturbation. In the quadrotor configuration studied, weathercock stability arises from asymmetries in rotor torque response under sideslip conditions. Specifically, when a lateral disturbance occurs, the rotor vortex wakes are deflected obliquely downstream, with Rotor 3 experiencing the most pronounced disturbance (see Figure 13). This asymmetric wake interaction results in an increase in torque on the affected rotor, producing an additional yawing moment in the direction of the sideslip. The interference-induced yaw moment thus enhances the aircraft's $\bar{N}_v$. This mechanism serves as a multirotor analogue to the stabilizing contributions from tail fins or fuselage side force generation in conventional rotorcraft, as discussed in Padfield [4], Chapter 4. The result underscores the importance of wake-induced torque coupling in defining lateral-directional static stability in multirotor designs.

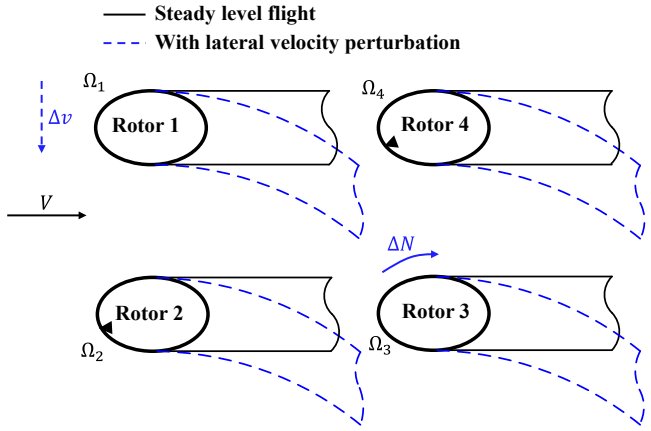

Figure 13 Impact of lateral velocity perturbation on yaw moment.

Figure 14 presents the variation of key damping derivatives— $\bar{L}_p$, $\bar{N}_r$, $\bar{M}_q$ and $\bar{Z}_w$ —across a range of forward flight speeds, comparing scenarios with and without multirotor aerodynamic interference.

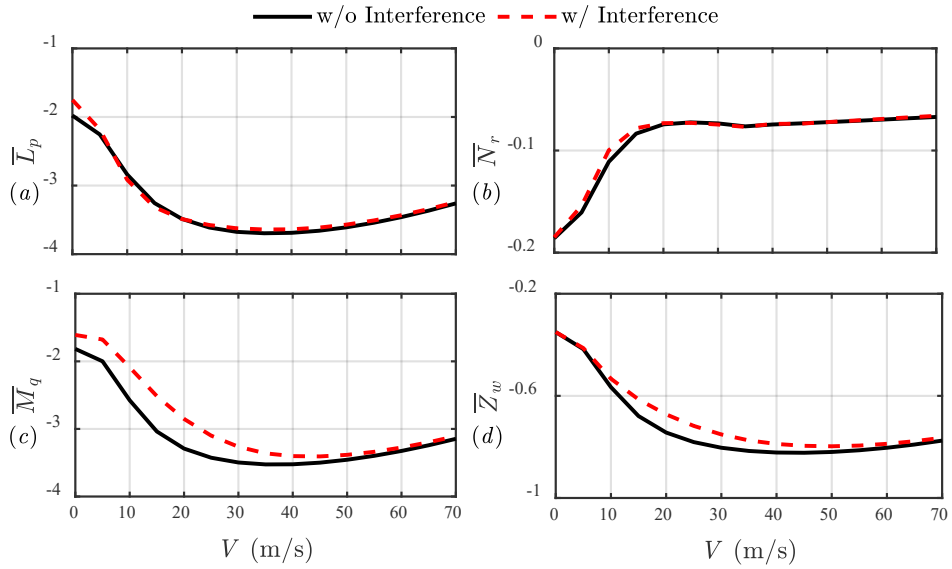

Figure 14 Comparison of damping derivatives with flight speed: (*a*) roll-damping derivative ($\bar{L}_p$), (*b*) yaw-damping derivative ($\bar{N}_r$), (*c*) pitch-damping derivative ($\bar{M}_q$), and (*d*) heave-damping derivative ($\bar{Z}_w$).

Figure 14 (*a*) shows that the roll-damping derivative $\bar{L}_p$ remains largely unaffected by interference across the flight envelope. The close agreement between the interference and non-interference cases suggests that roll damping, dominated by symmetric rotor contributions, is relatively insensitive to wake interaction effects in this configuration. In Figure 14 (*b*), the yaw-damping derivative $\bar{N}_r$ exhibits similarly weak sensitivity to interference. A modest increase in yaw-damping is observed at low speeds with interference, likely resulting from slight asymmetries in rotor wake interactions under yaw-rate perturbations. However, the overall influence remains limited, consistent with the yaw-damping behavior of other symmetric multirotor systems.

In contrast, Figure 14 (*c*) reveals that the pitch-damping derivative $\bar{M}_q$ is notably affected by aerodynamic interference, particularly at low to moderate speeds. The increased damping in the interference case reflects the delayed response of rotor wakes to pitch-rate inputs, as illustrated in Figure 15. As the vehicle pitches, the wake from the front rotors increasingly interacts with the rear rotors, generating additional stabilizing moments. This dynamic interaction enhances pitch damping, although the effect diminishes with increasing speed as wake structures become more aligned and less coupled. Figure 14 (*d*) illustrates a similar trend for the heave-damping derivative $\bar{Z}_w$. Here, aerodynamic interference strengthens the damping across much of the speed range. This increase is attributed to wake

accumulation beneath the vehicle during vertical motion, which induces greater aerodynamic resistance, especially on the rotor opposing the direction of travel. As with pitch damping, the effect of interference subsides at higher speeds due to reduced wake residence time in the flow field.

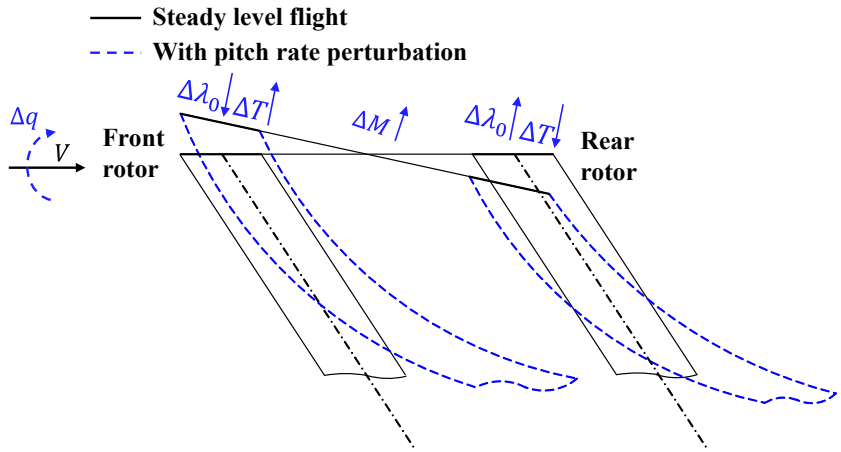

Figure 15 Impact of pitch rate on pitch moment.

In summary, the developed flight dynamics model successfully captures the influence of multirotor aerodynamic interference on both static and damping derivatives across the full range of flight conditions. By incorporating wake interaction effects between rotors, the model reveals critical axis-dependent stability trends—most notably, the enhancement of longitudinal and vertical damping, and the degradation of incidence stability in low-speed regimes. These findings provide a more physically grounded understanding of multirotor dynamic behavior and serve as a robust theoretical foundation for subsequent analyses of stability margins and HQs. The ability to resolve such interference-driven effects is particularly important for accurate prediction of eVTOL performance under ADS-33E-PRF-based handling criteria, especially in transitional and low-speed flight regimes, where wake coupling is most pronounced.

2. Dynamic stability

The dynamic stability analysis investigates the influence of multirotor aerodynamic interference on the root locus distribution for both longitudinal and lateral-directional modes, as shown in Figure 16 and Figure 17. The plots compare modal eigenvalues between hover (0 m/s, denoted by ‘x’) and cruise flight (70 m/s, represented by ‘o’), demonstrating the speed-dependent variations in stability characteristics.

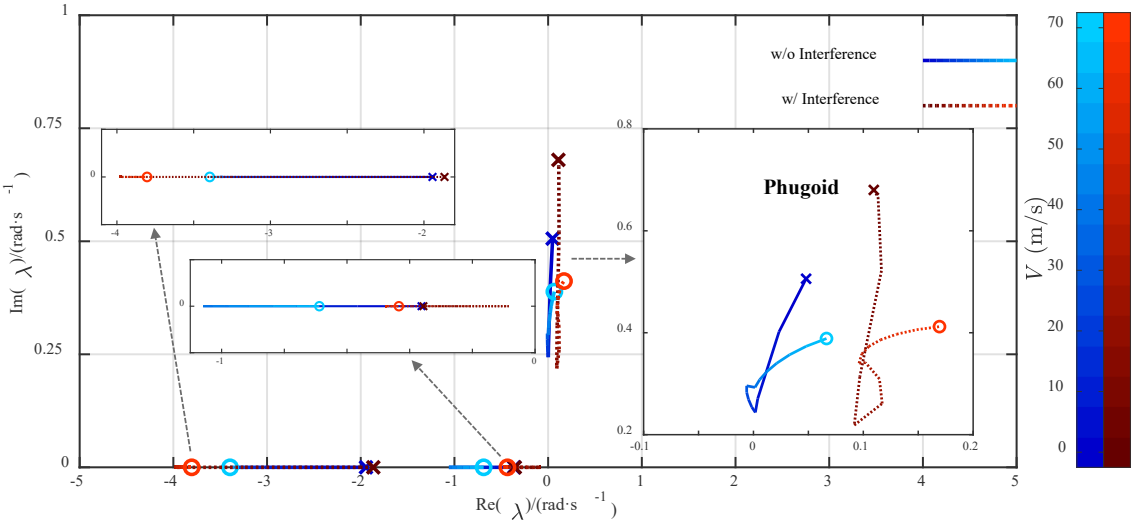

Figure 16 Root locus distribution of longitudinal modes with flight speed.

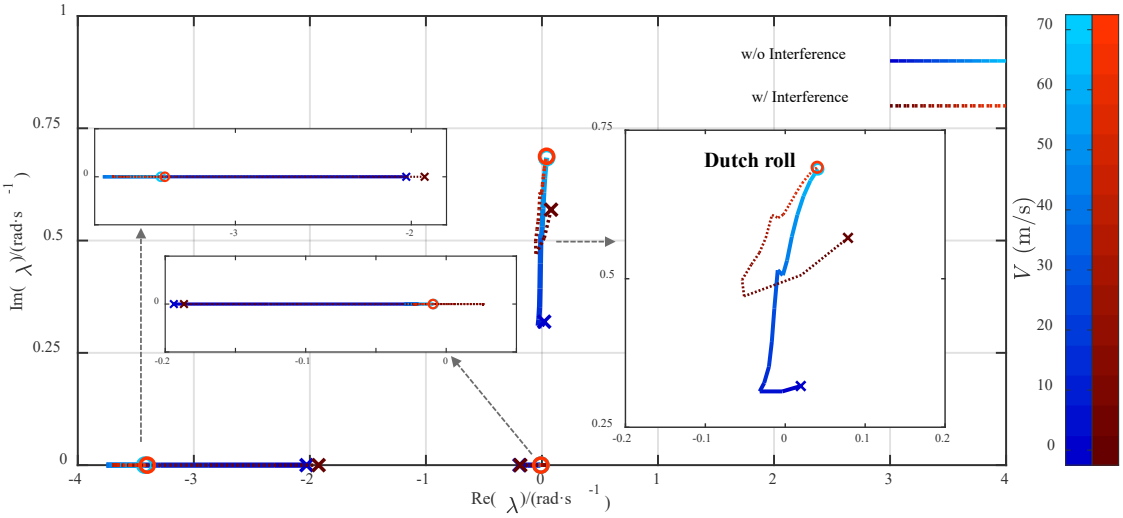

Figure 17 Root locus distribution of lateral-directional modes with flight speed.

Figure 16 illustrates that the classical short-period mode decomposes into two distinct aperiodic modes: pitch subsidence and heave subsidence. This behavior can be attributed to the absence of a horizontal tailplane, which, in conventional fixed-wing aircraft, provides significant pitch stiffness and plays a key role in sustaining the short-period's characteristic oscillatory dynamics. The figure reveals that the pitch subsidence mode is characterized by larger negative real roots, while the heave mode exhibits smaller negative real roots. In the low-to-moderate speed regime, multirotor aerodynamic interference causes rightward shifts in the root loci for both modes, thereby degrading their stability. These findings are consistent with the trends observed in Figure 14, which shows significant reductions in both $\bar{M}_q$ and $\bar{Z}_w$ at a similar speed range. The phugoid mode is represented by a pair of complex conjugate roots with relatively small real components, exhibiting slow damping and oscillatory characteristics. Multirotor

aerodynamic interference induces a substantial rightward shift in the phugoid mode's root loci, markedly degrading its stability. This destabilization primarily stems from multirotor interference-induced variations in $\bar{M}_w$.

Figure 17 illustrates that the roll subsidence mode is characterized by a large negative real eigenvalue, while the spiral mode exhibits a smaller negative real eigenvalue. Notably, multirotor aerodynamic interference destabilizes the spiral mode at low-to-medium speeds, causing its root to transition from the stable left-half plane to the unstable right-half plane. This destabilization primarily results from the strong coupling between $\bar{N}_v$ and spiral mode stability, where the interference-induced enhancement of $\bar{N}_v$ adversely affects spiral mode characteristics.

The Dutch roll mode exhibits a non-monotonic stability trend—transitioning from unstable to stable and then becoming unstable again—as forward speed increases, even in the absence of multirotor aerodynamic interference. This behavior reflects the inherent lateral-directional dynamics of the vehicle, rather than being solely a product of wake interactions. The observed trend is driven by the competing effects of yaw stiffness $\bar{N}_v$, yaw damping $\bar{N}_r$, and the dihedral effect $\bar{L}_v$, all of which evolve differently with flight speed. At low speeds, weak aerodynamic damping combined with limited directional stability can result in an unstable Dutch roll mode. As speed increases, body-generated side forces and rotor-induced dihedral effects strengthen, providing temporary stabilization. However, at higher speeds, yaw stiffness may again grow disproportionately—particularly in the absence of a vertical stabilizer—while yaw damping tends to plateau or diminish, reintroducing instability. This behavior underscores the sensitivity of Dutch roll dynamics to subtle changes in aerodynamic and inertial coupling, even in interference-free conditions.

B. Handling qualities analysis

The nonlinear flight dynamics model is employed to simulate the aircraft's dynamic response to prescribed control inputs. The response characteristics are analyzed to assess the aircraft's HQs, which are quantitatively evaluated using the ADS-33E-PRF performance standards. Building on this framework, the study systematically investigates both the underlying mechanisms and the magnitude of multirotor aerodynamic interference effects on the vehicle's HQs.

1. Bandwidth/phase delay

The bandwidth/phase delay criterion, as defined in ADS-33E-PRF HQs standards, provides a quantitative assessment of the aircraft's attitude response characteristics to small-amplitude control inputs (typically ±10% of full control deflection). Figure 18 demonstrates the influence of multirotor aerodynamic interference on attitude bandwidth characteristics during hover, medium-speed ($\mu = 0.11$), and high-speed ($\mu = 0.29$) flight conditions. The roll bandwidth,

as presented in Figure 18 (*a*), consistently remains within the Level 2 region across all advance ratios. The multirotor aerodynamic interference exhibits negligible effect on achievable roll bandwidth, a finding that aligns with and corroborates the preceding stability derivative analysis.

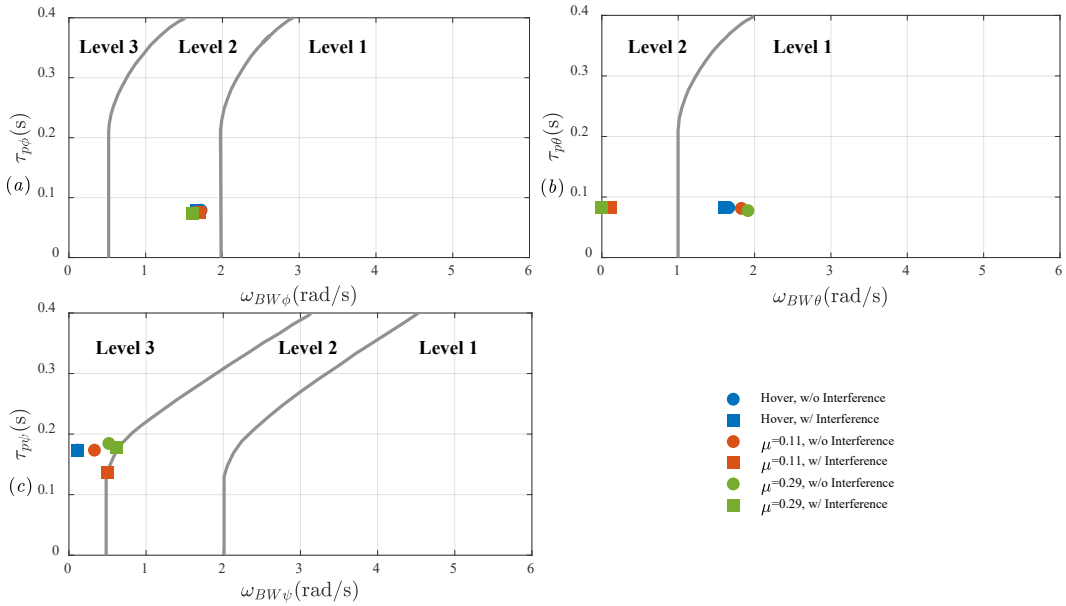

Figure 18 Bandwidth/phase delay results for each axis under varying flight conditions. (*a*) Roll bandwidth, (*b*) Pitch bandwidth, (*c*) Yaw bandwidth, with the influence of multirotor aerodynamic interference.

Figure 18 (*b*) shows that the pitch bandwidth remains within the Level 1 region when neglecting multirotor interference effects. However, when accounting for aerodynamic interference, the pitch bandwidth degrades significantly to Level 2 during medium- and high-speed forward flight. This reduction is primarily driven by aerodynamic interference, which causes $\bar{M}_w$ to become positive, thereby reducing the natural frequency of the short-period mode. More critically, for the quadrotor configuration considered, the classical short-period oscillation breaks down entirely, decomposing into two distinct aperiodic modes—heave and pitch subsidence—as previously discussed.

Figure 18 (*c*) demonstrates that the yaw bandwidth initially resides in the Level 2/3 regions, indicating suboptimal yaw control authority. The analysis shows that multirotor aerodynamic interference enhances $\bar{N}_v$, which in turn improves the dynamic response characteristics. This stability augmentation elevates the yaw bandwidth from Level 3 to approach the Level 2 boundary during medium- to high-speed forward flight conditions.

2. Dynamic stability

Figure 19 presents the dynamic stability assessment for both pitch and roll axes, showing that multirotor aerodynamic interference degrades Phugoid mode stability from Level 1 to Level 2 while reducing Dutch roll mode

stability from Level 1 to near the Level 1/2 boundary. This degradation indicates a substantial deterioration in both dynamic response capability and oscillation damping characteristics, exhibiting strong agreement with the predicted stability trends in Figure 16 and Figure 17.

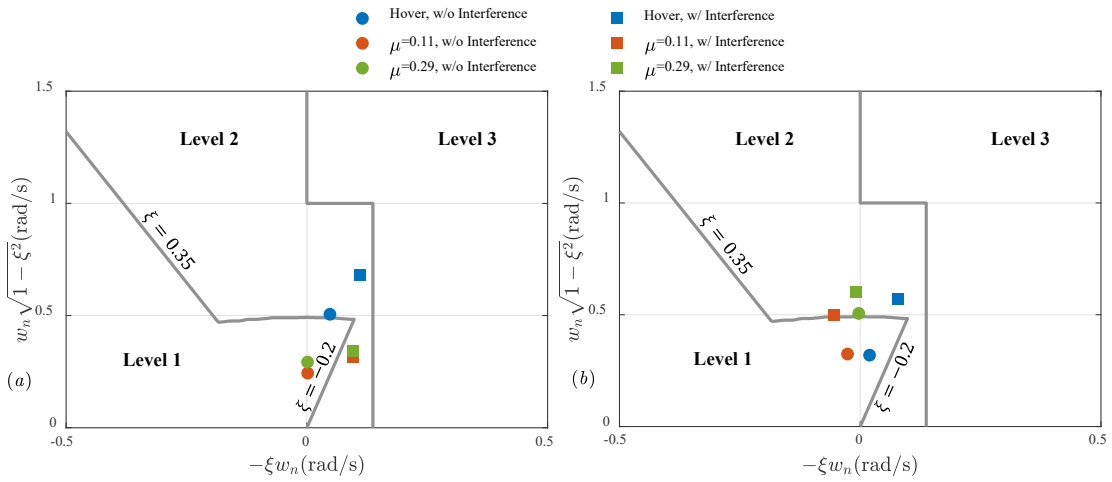

Figure 19 Dynamic stability characteristics of (*a*) the Phugoid mode and (*b*) the Dutch roll mode.

3. Attitude quickness

Attitude quickness serves as a key metric for characterizing aircraft responsiveness to moderate-amplitude control inputs (typically 20-50% of full control deflection). As illustrated in Figure 20, the pitch response (both attitude and rate) to a moderate longitudinal control input demonstrates this dynamic characteristic. The pitch channel quickness is quantitatively defined as the ratio of peak pitch rate (q_{peak}) to the resultant pitch attitude change ($\Delta\theta$), with an analogous formulation applying to the roll channel (p_{peak} / $\Delta\phi$) for lateral-directional assessment.

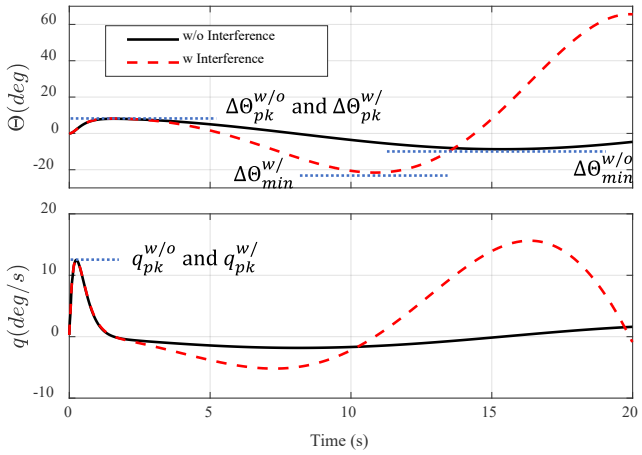

Figure 20 Pitch attitude and rate responses for attitude quickness evaluation.

Figure 21 presents the attitude quickness characteristics for both pitch and roll axes. The results indicate that both axes consistently satisfy Level 1 HQs requirements across the evaluated flight envelope. However, pitch-axis quickness progressively decreases with increasing forward speed, a trend primarily driven by enhanced static stability at higher speeds, which reduces the aircraft's responsiveness to moderate control inputs. Notably, multirotor aerodynamic interference leads to a measurable improvement in pitch-axis quickness. This enhancement is directly attributable to the reduction in the incidence stability derivative $\bar{M}_w$, which, as previously discussed, becomes positive under interference, thereby increasing the initial pitch rate response for a given control input.

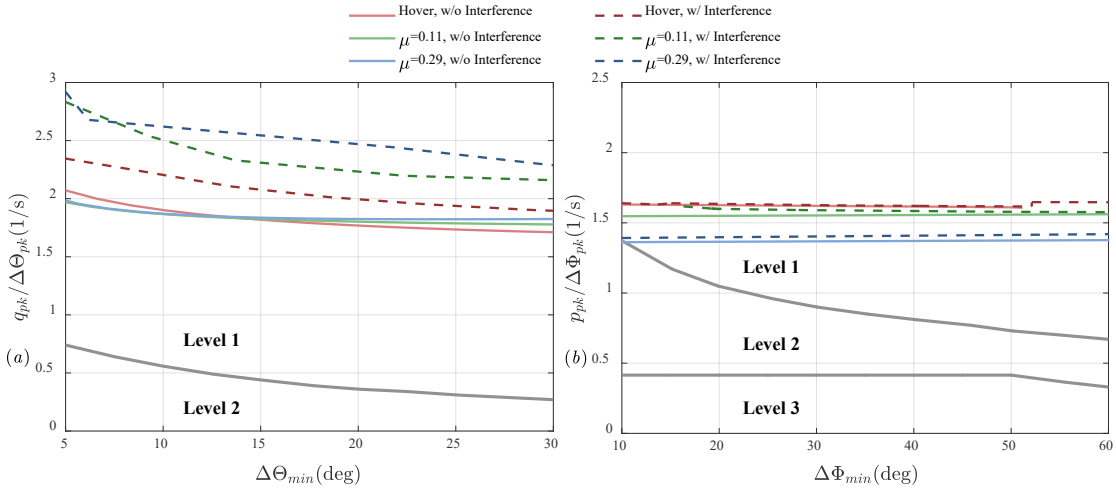

Figure 21 Attitude quickness results for (*a*) pitch axis and (*b*) roll axis.

4. Axes coupling

Axis coupling describes the unintended control interactions that occur when command inputs to one primary control axis induce responses in other axes. Figure 22 shows that the aircraft's symmetrical airframe design ensures minimal cross-axis coupling (roll-pitch, pitch-roll, and yaw-heave interactions) throughout the operational control amplitude range, consistently meeting Level 1 HQ standards. The system maintains excellent axis decoupling performance, with coupling effects remaining within negligible levels despite multirotor aerodynamic interference.

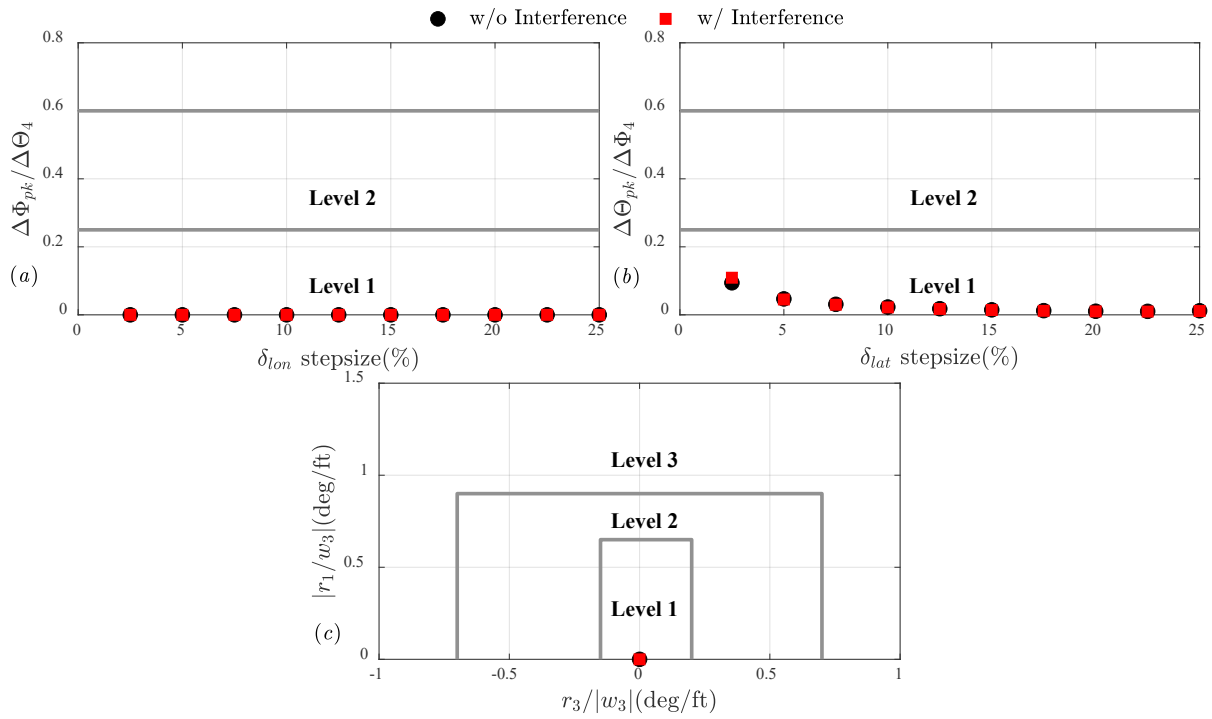

Figure 22 Cross-axis coupling for (*a*) roll-pitch, (*b*) pitch-roll, and (*c*) yaw-heave interactions.

5. Height response

The height response is characterized by the vertical velocity response of the aircraft within 5 seconds following a collective control step input. Figure 23 shows that the height response under all advance ratios is classified within Level 1 performance. The multirotor aerodynamic interference leads to an increased time constant at medium to high forward speeds due to the reduced eigenvalue of the heave mode, as illustrated in Figure 16.

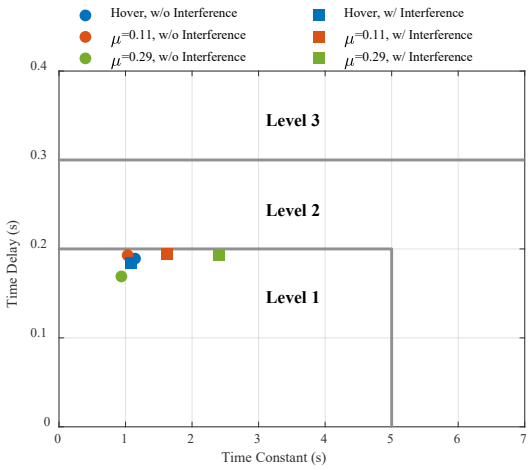

Figure 23 Height response evaluation results.

VI Discussion

This study presents an efficient alternative to computationally intensive CFD and vortex methods for analyzing multirotor aerodynamic interference. Although high-fidelity simulations can accurately characterize these effects, their practical implementation faces significant challenges due to excessive computational demands and difficulties in isolating individual interference components—essential for flight dynamics analysis [60]. The developed approach combines a dynamical rotor vortex tube model with dynamic inflow theory, effectively capturing vehicle angular motion effects while maintaining the computational efficiency required for engineering applications. Validation against wind tunnel data shows a strong correlation, with rotor interference predictions maintaining maximum errors below 15%, satisfying flight dynamics simulation accuracy requirements.

The integrated modeling framework incorporates blade flapping dynamics with the enhanced inflow representation, creating a comprehensive quadrotor eVTOL flight dynamics model that accurately reproduces multirotor coupling effects. Trim analysis conducted across the complete forward flight range (0 - 70 m/s) demonstrates the model's robust predictive capability, exhibiting only 8% maximum deviation from reference data. These results verify the model's capacity to reliably assess both performance characteristics and HQs variations induced by aerodynamic interference, establishing its practical utility for eVTOL design and development processes.

The effects of multirotor aerodynamic interference on eVTOL stability and HQs were investigated. The analysis reveals that aerodynamic interference simultaneously increases incidence stability static instability while improving speed static stability, significantly degrading phugoid mode stability. At low-to-medium speeds, reduced pitch and vertical damping compromise both pitch subsidence and heave mode stability. Lateral-directional behavior exhibits speed-dependent characteristics, where enhanced static stability destabilizes the spiral mode while the Dutch roll mode shows improved stability at low speeds (indicated by leftward root locus shift) that transitions to reduced stability (rightward migration) above a critical speed.

The interference substantially impacts HQs, particularly degrading pitch bandwidth from Level 1 to Level 2 at medium-high speeds and reducing dynamic stability in both pitch and roll axes to Level 2. While pitch channel quickness improves noticeably and roll quickness shows marginal enhancement, the effects on axes coupling and heave response remain negligible. These findings quantitatively demonstrate how multirotor interference fundamentally modifies eVTOL HQs, underscoring the necessity to incorporate these effects in aircraft development to maintain optimal performance across the flight envelope.

VII Conclusions

This paper introduced and validated a comprehensive flight dynamics model for a quadrotor eVTOL aircraft, explicitly accounting for multirotor aerodynamic interference through a dynamic vortex tube approach. Integrated with rotor flapping and 6-DoF dynamics, the model accurately predicts interference-driven impacts on trim, stability, and HQs throughout the flight envelope. The analysis highlights the significant influence of rotor wake interactions on stability characteristics, underscoring their importance in HQs evaluation and flight control design. The key findings are:

- Multirotor aerodynamic interference substantially reduces longitudinal and incidence stability, particularly at low to moderate speeds, driven by wake-induced coupling effects between rotors.
- The Dutch roll mode exhibits non-monotonic stability behavior, oscillating between stable and unstable regions as speed increases, reflecting intricate interactions between yaw damping and yaw stiffness inherent to the quadrotor configuration.
- HQs assessments (ADS-33E-PRF) reveal clear interference-related degradations in pitch bandwidth and dynamic stability, alongside improvements in pitch-axis quickness, demonstrating the complexity of interference effects on overall control responsiveness.

Future research will extend the developed methodology to more complex eVTOL configurations, including tilt-rotor and distributed propulsion systems. Additionally, incorporating higher-fidelity, transient aerodynamic modeling and pilot-in-the-loop simulations will further strengthen the framework, providing more comprehensive support for eVTOL design optimization and certification processes.

Funding Sources

This research was supported by the National Natural Science Foundation of China, NO: 11902052; the Natural Science Foundation of Chongqing, NO: CSTB2022NSCQ-MSX1592; the Rotor Aerodynamics Key Laboratory, China Aerodynamics Research and Development Center, NO: RAL202302-3.

References

[1] F. Mazzeo, M.D. Pavel, D. Fattizzo, G. Bertolani, E.L. de Angelis, F. Giulietti, Flight dynamic modeling and stability of a small-scale side-by-side helicopter for Urban Air Mobility, Aerospace Science and Technology, 148 (2024) 109117. doi: 10.1016/j.ast.2024.109117.

[2] C. Silva, W.R. Johnson, E. Solis, M.D. Patterson, K.R. Antcliff, VTOL urban air mobility concept vehicles for technology development, 2018 Aviation Technology, Integration, and Operations Conference, 2018, pp. 3847.

[3] H. Li, Z. Kan, D. Bie, D. Li, S. Zhao, Aerodynamic interference analysis of multiple rotors in a heterogeneous unmanned aircraft system, Physics of Fluids, 35 (2023) 115120. doi: 10.1063/5.0174331.

[4] G.D. Padfield, Helicopter flight dynamics: including a treatment of tiltrotor aircraft, John Wiley & Sons2018.

[5] G.D. Padfield, Rotorcraft handling qualities engineering: managing the tension between safety and performance 32nd alexander a. nikolsky honorary lecture, Journal of the American Helicopter Society, 58 (2013) 1-27. doi: 10.4050/JAHS.58.011001.

[6] S. Herz, A. Atte, D. Seth, J. Rauleder, M. McCrink, Effects of rotor–rotor and rotor–body interactions on quadrotor vehicle performance for multiple flight configurations, Aerospace Science and Technology, 158 (2025) 109873. doi: 10.1016/j.ast.2024.109873.

[7] A. Zanotti, A. Velo, C. Pepe, A. Savino, D. Grassi, L. Riccobene, Aerodynamic interaction between tandem propellers in eVTOL transition flight configurations, Aerospace Science and Technology, 147 (2024) 109017. doi: 10.1016/j.ast.2024.109017.

[8] Y. Yuan, R. Chen, P. Li, Trim investigation for coaxial rigid rotor helicopters using an improved aerodynamic interference model, Aerospace Science and Technology, 85 (2019) 293-304. doi: 10.1016/j.ast.2018.11.044.

[9] H. Qi, G. Xu, C. Lu, Y. Shi, A study of coaxial rotor aerodynamic interaction mechanism in hover with high-efficient trim model, Aerospace Science and Technology, 84 (2019) 1116-1130. doi: 10.1016/j.ast.2018.11.053.

[10] V.K. Lakshminarayan, J.D. Baeder, High-resolution computational investigation of trimmed coaxial rotor aerodynamics in hover, Journal of the American Helicopter Society, 54 (2009) 42008-42008. doi: 10.4050/JAHS.54.042008.

[11] L. Ye, Y. Zhang, S. Yang, X. Zhu, J. Dong, Numerical simulation of aerodynamic interaction for a tilt rotor aircraft in helicopter mode, Chinese Journal of aeronautics, 29 (2016) 843-854. doi: 10.1016/j.cja.2016.06.001.

[12] J.Y. Hwang, M.K. Jung, O.J. Kwon, Numerical study of aerodynamic performance of a multirotor unmanned-aerial-vehicle configuration, Journal of Aircraft, 52 (2015) 839-846. doi: 10.2514/1.C032828.

[13] M. Misiorowski, F. Gandhi, A.A. Oberai, Computational study on rotor interactional effects for a quadcopter in edgewise flight, AIAA Journal, 57 (2019) 5309-5319. doi: 10.2514/1.J058369.

[14] A. Stoll, G.V. Miki, Transition performance of tilt propeller aircraft, 78th Vertical Flight Society Annual Forum and Technology Display, FORUM 2022, May 10, 2022 - May 12, 2022, Vertical Flight Society, Fort Worth, TX, United states, 2022.

[15] A. Bagai, J.G. Leishman, Free‐Wake analysis of tandem, tilt‐rotor and coaxial rotor configurations, Journal of the American Helicopter Society, 41 (1996) 196-207. doi: 10.4050/JAHS.41.196.

[16] J. Lee, K. Yee, S. Oh, Aerodynamic characteristic analysis of multi-rotors using a modified free-wake method, Transactions of the Japan Society for Aeronautical and Space Sciences, 52 (2009) 168-179. doi: 10.2322/tjsass.52.168.

[17] E.J. Alvarez, A. Ning, High-fidelity modeling of multirotor aerodynamic interactions for aircraft design, AIAA Journal, 58 (2020) 4385-4400. doi: 10.2514/1.J059178.

[18] R.E. Brown, Rotor wake modeling for flight dynamic simulation of helicopters, AIAA Journal, 38 (2000) 57-63. doi: 10.2514/2.922.

[19] T.M. Fletcher, R.E. Brown, Helicopter tail rotor thrust and main rotor wake coupling in crosswind flight, Journal of aircraft, 47 (2010) 2136-2148. doi: 10.2514/1.C031018.

[20] D. Usov, W. Appleton, A. Filippone, N. Bojdo, Low-order aerodynamic model for interference in multirotor systems, Journal of Aircraft, 59 (2022) 1450-1462. doi: 10.2514/1.C036797.

[21] J. Luo, L. Zhu, G. Yan, Novel quadrotor forward-flight model based on wake interference, Aiaa Journal, 53 (2015) 3522-3533. doi: 10.2514/1.J053011.

[22] D. Han, G.N. Barakos, Aerodynamic interference model for multirotors in forward flight, Journal of Aircraft, 57 (2020) 1220-1223. doi: 10.2514/1.C035978.

[23] M. Divaker, Equivalent wing numerical lifting line theory for predicting rotor performance and rotor-rotor interference, University of Florida, 2021, pp. 48-60.

[24] F. Guner, J. Prasad, Combined momentum theory and simple vortex theory inflow model for multirotor configurations, Journal of the American Helicopter Society, 67 (2022) 1-15. doi: 10.4050/JAHS.67.022007.

[25] A.J. Ruddell, Advancing blade concept (ABC™) development, Journal of the American Helicopter Society, 22 (1977) 13-23. doi: 10.4050/JAHS.22.1.13.

[26] A. Ruddell, J. Macrino, Advancing blade concept (ABC) high speed development, American Helicopter Society 36th Annual Forum, Washington, DC, 1980, pp. 1-13.

[27] O. Rand, V. Khromov, Free-wake–based dynamic inflow model for hover, forward, and maneuvering flight, Journal of the American Helicopter Society, 63 (2018) 1-16. doi: 10.4050/JAHS.63.012008.

[28] O. Rand, V. Khromov, Parametric study of dynamic inflow for single and coaxial rotor systems, Journal of the American Helicopter Society, 63 (2018) 1-14. doi: 10.4050/JAHS.63.042007.

[29] S. Park, B. Im, D. Lee, S. Shin, Aerodynamic interference analysis for a nonoverlapping multirotor UAV based on dynamic vortex tube, Journal of the American Helicopter Society, 68 (2023) 42010-42030. doi: 10.4050/JAHS.68.042010.

[30] P. Singh, P.P. Friedmann, Application of vortex methods to coaxial rotor wake and load calculations, 55th AIAA Aerospace Sciences Meeting, 2017, pp. 0051.

[31] D. Agarwal, L. Lu, G.D. Padfield, M.D. White, N. Cameron, The use of augmented rotor inflow to predict rotorcraft responses in hover and low-speed manoeuvres, The Aeronautical Journal, 126 (2022) 1168-1186. doi: 10.1017/aer.2021.123.

[32] Y.-B. Kong, J. Prasad, L.N. Sankar, C. He, Finite state inflow flow model for coaxial rotor configuration, Journal of the American Helicopter Society, 65 (2020) 1-11. doi: 10.4050/JAHS.65.032002.

[33] F. Guner, J. Prasad, D.A. Peters, An Approximate Finite State Dynamic Wake Model for Predictions of Inflow below the Rotor, Journal of the American Helicopter Society, 66 (2021) 1-10. doi: 10.4050/JAHS.66.032007.

[34] Y.-B. Kong, J. Prasad, C. He, Finite state coaxial rotor inflow model enhancements using VVPM-extracted influence coefficients, Journal of the American Helicopter Society, 65 (2020) 1-17. doi: 10.4050/JAHS.65.022008.

[35] F. Guner, J. Prasad, C. He, D. Peters, Fidelity enhancement of a multirotor dynamic inflow model via system identification, Journal of the American Helicopter Society, 67 (2022) 1-17. doi: 10.4050/JAHS.67.022009.

[36] S. Suvarna, H. Chung, A. Sinha, R.S. Pant, Revised semi-empirical aerodynamic estimation for modelling flight dynamics of an airship, Aerospace Science and Technology, 126 (2022) 107642. doi: 10.1016/j.ast.2022.107642.

[37] W. Johnson, C. Silva, NASA concept vehicles and the engineering of advanced air mobility aircraft, The Aeronautical Journal, 126 (2022) 59-91. doi: 10.1017/aer.2021.92.

[38] K. Atci, T. Jusko, A. Štrbac, F. Guner, Impact of differential torsional rotor cant on the flight characteristics of a passenger-grade quadrotor, CEAS Aeronautical Journal, 15 (2024) 513-528. doi: 10.1007/s13272-023-00705-7.

[39] D. Milz, G. Looye, Tilt-wing control design for a unified control concept, AIAA Scitech 2022 forum, 2022, pp. 1084.

[40] A. Walter, M. McKay, R. Niemiec, F. Gandhi, T. Berger, Hover dynamics and flight control of a UAM-scale quadcopter with hybrid rpm and collective pitch control, Journal of the American Helicopter Society, 68 (2023) 143-160. doi: 10.4050/JAHS.68.022012.

[41] H. Glauert, Airplane Propellers in Aerodynamic Theory, Springer, Berlin, Heidelberg, 1935, pp. 169-360.

[42] H.H. Heyson, Equations for the induced velocities near a lifitng rotor with nonuniform azimuthwise vorticity distribution, NASA TND-394, 1960.

[43] J. Zhao, Dynamic wake distortion model for helicopter maneuvering flight, Georgia Institute of Technology, 2005.

[44] G.H. Vatistas, New model for intense self-similar vortices, Journal of Propulsion and Power, 14 (1998) 462-469. doi: 10.2514/2.5323.

[45] D.A. Peters, N. HaQuang, Dynamic inflow for practical applications, Journal of American Helicopter Society, 33 (1988) 64-68. doi: 10.4050/JAHS.33.64.

[46] H. Ji, R. Chen, P. Li, Rotor-state feedback control to alleviate pilot workload for helicopter shipboard operations, Journal of Guidance, Control, and Dynamics, 40 (2017) 3088-3099. doi: 10.2514/1.G002304.

[47] H. Ji, L. Lu, M.D. White, R. Chen, Advanced pilot modeling for prediction of rotorcraft handling qualities in turbulent wind, Aerospace Science and Technology, 123 (2022) 107501. doi: 10.1016/j.ast.2022.107501.

[48] R.T. Chen, A simplified rotor system mathematical model for piloted flight dynamics simulation, No. NASA-TM-78575, 1979.

[49] C. Malpica, S. Withrow-Maser, Handling qualities analysis of blade pitch and rotor speed controlled eVTOL quadrotor concepts for urban air mobility, VFS international powered lift conference, San Jose, CA, 2020, pp. 21-23.

[50] H. Ji, R. Chen, P. Li, Real-time simulation model for helicopter flight task analysis in turbulent atmospheric environment, Aerospace Science and Technology, 92 (2019) 289-299. doi: 10.1016/j.ast.2019.05.066.

[51] H. Ji, R. Chen, L. Lu, M.D. White, Pilot workload investigation for rotorcraft operation in low-altitude atmospheric turbulence, Aerospace Science and Technology, 111 (2021) 106567. doi: 10.1016/j.ast.2021.106567.

[52] H. Ji, R. Chen, P. Li, Distributed atmospheric turbulence model for helicopter flight simulation and handling-quality analysis, Journal of Aircraft, 54 (2017) 190-198. doi: 10.2514/1.C033667.

[53] Q. Kang, H. Ji, Y. Yuan, Y. Ye, Autonomous helicopter shipboard recovery flight control design based on tau theory, Aerospace Science and Technology, 159 (2025) 109956. doi: 10.1016/j.ast.2025.109956.

[54] R.C. Dingeldein, Wind-tunnel studies of the performance of multirotor configurations, NACA Note 3236, 1954.

[55] J.G. Leishmann, Principles of helicopter aerodynamics, 2006.

[56] S. Huang, Theoretical and experimental research on aerodynamic interaction characteristics for tandem twin-rotor helicopters, Nanjing University of Aeronautics and Astronautics, 2009 (in Chinese).

[57] W. Johnson, C. Silva, E. Solis, Concept vehicles for VTOL air taxi operations, AHS Specialists' Conference on Aeromechanics Design for Transformative Vertical Flight, 2018.

[58] K. Atci, M. Jones, T. Jusko, Assessment of the handling qualities of multirotor configurations using real time simulation, (2021). doi: 10.25967/550236.

[59] ADS-33E-PRF aeronautical design standard performance specification handling qualities requirements for military rotorcraft, United States Army Aviation and Missile Command Aviation Engineering Directorate, Redstone Arsenal, Alabama, 2000.

[60] L. Lu, G. Padfield, M. White, P. Perfect, Fidelity enhancement of a rotorcraft simulation model through system identification, The Aeronautical Journal, 115 (2011) 453-470. doi: 10.1017/S0001924000006102.

Modeling multirotor wake interference in quadrotor eVTOL flight dynamics and handling qualities

Wang, Yeping

2025-10-01

Wang Y, Ji H, Lu L, Zhou P. (2025) Modeling multirotor wake interference in quadrotor eVTOL flight dynamics and handling qualities. Aerospace Science and Technology, Volume 165, October 2025, Article number 110533

https://doi.org/10.1016/j.ast.2025.110533